Direct simulation of gas–surface interaction in a turbulent reacting hypersonic boundary layer

By C. T. Williams, M. Di Renzo†, M. Panesi‡ AND P. Moin

Gas–surface interaction within a Mach 7 hypersonic boundary layer overriding a 3000 K graphite substrate is characterized with direct numerical simulation (DNS). Owing to instantaneous fluctuations in near-wall radical species, near-wall turbulent structures produce local variations in the ablative mass flux that exceed an order of magnitude. With a surface chemical mechanism composed of oxidation, nitridation, recombination, and sublimation processes, the presence of surface chemistry strongly modulates near-wall thermodynamics and gas-phase chemical production rates relative to a noncatalytic boundary layer counterpart. In particular, nearly all near-wall atomic radical species are depleted via surface chemical reactions, producing an ablation product boundary layer with significant concentrations of carbon monoxide. Owing to this consumption of atomic oxygen at the graphite surface, an off-wall peak in atomic oxygen variance emerges within the aerodynamic heating layer. This modulation of the near-wall chemical composition by gas–surface interactions also strongly affects the gas-phase chemical production rates of all major species in the turbulent hypersonic boundary layer relative to its noncatalytic counterpart, as mediated by both dissociation/recombination phenomena and exchange reactions.

1. Introduction

The hypersonic flight environment subjects reentry vehicles to significant aerodynamic heating, owing to the combined presence of hydrodynamic phenomena such as viscous dissipation in high-speed boundary layers, shock-interference heating, and shock–boundary layer interactions (Bertin & Cummings 2006; Urzay 2018; Urzay & Di Renzo 2021). The high temperatures introduced by these phenomena activate several nonequilibrium physicochemical processes in hypersonic shock layers, including finite-rate relaxation of rovibrational and electronic internal energy modes, dissociation/recombination processes among diatomic molecules, and the formation of charged species through ionization reactions and nitric oxide via the Zel'dovich mechanism (Vincenti & Krüger 1965; Zel'dovich & Raizer 2002; Candler 2019). Together with the emergence of gas-phase aerothermochemistry, the elevated near-wall temperatures characteristic of hypersonic flow likewise activate complex gas–surface chemical processes such as recombination, oxidation, nitridation, and sublimation (Park 1990; Candler 2019). In addition to mediating the surface temperature of hypersonic vehicles through their heat of reaction, gas–surface reactions give rise to variations in gas-phase kinetics and thermophysical properties and, ultimately, the recession of the solid surface itself, ranging from large-scale deformation to smaller-scale surface patterning. The combination of ablation-induced surface roughness, wall-normal blowing, and thermal/compositional modulation of the boundary layer influ-

† Universitá del Salento
‡ University of California, Irvine

ences transition and convective heat transfer processes (Morkovin 1969; Schneider 2008, 2010).

With surface ablation rates determining the design of thermal protection systems and ultimately the survivability of high-speed flight vehicles, numerical simulation of gas–surface interaction has focused largely on laminar stagnation flows, representative of the leading-edge regions of high-speed flight systems where temperatures and ablation rates are highest (Keenan & Candler 1994; Olynick *et al.* 1997; Martin & Boyd 2015; McQuaid *et al.* 2025). Even in the absence of fluid instabilities, hypersonic ablation entails complex interactions among chemical processes, hydrodynamic motion, conjugate heat transfer, and thermal radiation (Engel *et al.* 1973; Gnoffo *et al.* 2010). For transitional hypersonic flows, gas–surface interaction and graphite ablation in particular can modify the growth of disturbances and breakdown to turbulence via several mechanisms, including modulation of boundary layer thermodynamics and molecular properties (Mortensen & Zhong 2014; Miró & Pinna 2020). The introduction of mass flux and nonzero transpiration at the ablative surface, particularly at high Mach numbers, likewise serves to accelerate laminar-to-turbulent transition hypersonic boundary layers through destabilization of second-mode waves (Mortensen & Zhong 2016; Miró & Pinna 2021).

With the breakdown to turbulence, the interaction between multiscale fluctuations and surface chemistry gives rise to a number of complex surface patterns, including so-called turbulent wedges, streamwise-aligned grooves, and cross-hatching structures (Canning *et al.* 1968*a*,*b*; Laganelli & Nestler 1969; Stock 1973). To date, however, numerical simulations of turbulent hypersonic flows with surface ablation have been limited to the Reynolds-averaged Navier–Stokes formalism (Thomas & Neier 1990; Komurasaki & Candler 2000; Lin *et al.* 2006; Bianchi *et al.* 2010), inherently neglecting turbulence–ablation interaction. To provide a high-fidelity characterization of gas–surface interaction in a turbulent reacting hypersonic boundary layer, in this study we present a preliminary DNS of Mach 7 flow over an ablative graphite surface, resolving all scales of turbulent motion.

The remainder of this brief is structured as follows. First, the formulation and physico-chemical modeling for the DNS are presented in Section 2. The corresponding mean-flow results for the ablative boundary layer computation are presented in Section 3. Finally, concluding remarks are provided in Section 4.

2. Formulation

For simulation of turbulent hypersonic gas–surface interaction, the multicomponent reacting Navier–Stokes equations are solved numerically with the HTR solver (Di Renzo *et al.* 2020). A low-dissipation, sixth-order hybrid skew-symmetric/TENO scheme (Williams *et al.* 2022) is used for the evaluation of inviscid fluxes, while the diffusive fluxes are evaluated with a second-order central discretization. Explicit time advancement is performed using a third-order strong-stability-preserving Runge–Kutta method (Gottlieb *et al.* 2001). Affording finite-rate evolution of reactive air species and ablation products, a continuity equation for each of the $N_s = 11$ species,

$$\frac{\partial \rho_\alpha}{\partial t} + \nabla\cdot(\rho_\alpha \mathbf{u}) = -\nabla\cdot(\rho_\alpha \boldsymbol{V_\alpha}) + \dot{w}_\alpha, \qquad \alpha = 1, ..., N_s, \tag{2.1}$$

is integrated numerically; here, ρ_α, $\dot{w}_\alpha$, and $\boldsymbol{V_\alpha}$ are the partial density, gas-phase chemical production rate, and diffusion velocity of species α, respectively. The overall set of species

considered for the dissociating air mixture with graphite ablation is given by

$$\alpha \in \{\mathrm{N_2}, \mathrm{O_2}, \mathrm{NO}, \mathrm{N}, \mathrm{O}, \mathrm{C}, \mathrm{C_2}, \mathrm{C_3}, \mathrm{CN}, \mathrm{CO}, \mathrm{CO_2}\}. \tag{2.2}$$

The gas-phase chemical reactions among these species, accounting for the dissociation/recombination of diatomic species as well as neutral exchange processes, is given by Park *et al.* (1994) as

$$\mathrm{N_2 + M \rightleftharpoons 2N + M}, \quad \text{(R1)} \qquad \mathrm{CO + C \rightleftharpoons C_2 + O}, \quad \text{(R11)}$$
$$\mathrm{O_2 + M \rightleftharpoons 2O + M}, \quad \text{(R2)} \qquad \mathrm{CO + O \rightleftharpoons O_2 + C}, \quad \text{(R12)}$$
$$\mathrm{NO + M \rightleftharpoons N + O + M}, \quad \text{(R3)} \qquad \mathrm{CO + N \rightleftharpoons CN + O}, \quad \text{(R13)}$$
$$\mathrm{N_2 + O \rightleftharpoons NO + N}, \quad \text{(R4)} \qquad \mathrm{N_2 + C \rightleftharpoons CN + N}, \quad \text{(R14)}$$
$$\mathrm{NO + O \rightleftharpoons O_2 + N}, \quad \text{(R5)} \qquad \mathrm{CN + O \rightleftharpoons NO + C}, \quad \text{(R15)}$$
$$\mathrm{C_2 + M \rightleftharpoons 2C + M}, \quad \text{(R6)} \qquad \mathrm{CN + C \rightleftharpoons C_2 + N}, \quad \text{(R16)}$$
$$\mathrm{CN + M \rightleftharpoons C + N + M}, \quad \text{(R7)} \qquad \mathrm{C_3 + N \rightleftharpoons CN + C_2}, \quad \text{(R17)}$$
$$\mathrm{CO + M \rightleftharpoons C + O + M}, \quad \text{(R8)} \qquad \mathrm{C_3 + C \rightleftharpoons 2C_2}, \quad \text{(R18)}$$
$$\mathrm{CO_2 + M \rightleftharpoons CO + O + M}, \quad \text{(R9)} \qquad \mathrm{CO_2 + O \rightleftharpoons CO + O_2}. \quad \text{(R19)}$$
$$\mathrm{CO + C_2 \rightleftharpoons C_3 + O}, \quad \text{(R10)}$$

In particular, reactions (R1)-(R3) and (R6)-(R9) represent dissociation/recombination among air and carbon-containing species, respectively, as mediated by a third-body collider M. Exchange reactions (R4)-(R5) constitute the Zel'dovich mechanism for nitric oxide formation, while reactions (R10)-(R19) represent the exchange processes among the ablation products. When all possible third-body collision partners entering into the dissociation/recombination reactions are accounted for, the total number of elementary reactions considered is $N_r = 89$. The rates and formulation for all of the air–species reactions are from Williams *et al.* (2023), while the gas-phase reaction rates for the ablation product species are evaluated with the parameterizations of Park *et al.* (1994). With the mean temperature in the boundary layer reaching only 5300 K, neglecting ionization processes and their products suffices for this study.

At the reactive surface, the balance of fluxes with surface chemical processes implies for each species α

$$(\rho_\alpha \boldsymbol{u} + \rho_\alpha \boldsymbol{V_\alpha}) \cdot \widehat{\boldsymbol{n}} = \dot{\Omega}_\alpha, \qquad \alpha = 1, ..., N_s, \tag{2.3}$$

where $\widehat{\boldsymbol{n}}$ is the wall-normal unit vector and $\dot{\Omega}_\alpha$ denotes the net production rate of species α via surface chemical reactions. This surface production rate can be expressed in terms of the species' partial densities as

$$\dot{\Omega}_\alpha = \mathcal{M}_\alpha \sum_\gamma \left(\nu''_{\alpha\gamma} - \nu'_{\alpha\gamma}\right) \left[\kappa_\gamma \prod_{\beta=1}^{N_s} \left(\frac{\rho_\beta}{\mathcal{M}_\beta}\right)^{\nu'_{\beta\gamma}}\right], \tag{2.4}$$

where $\mathcal{M}_\beta$ denotes the molecular mass of species β, and $\nu'_{\alpha\gamma}, \nu''_{\alpha\gamma} \in \mathbb{N}$ correspond to the reactant and product stoichiometric coefficients, respectively, for gas-phase species α in surface reaction γ. To represent graphite ablation, the following surface chemical

mechanism is utilized, where (s) denotes species that make up the solid surface,

$$\mathrm{C(s)} + \mathrm{O_2} \rightarrow \mathrm{CO} + \mathrm{O}, \tag{S1}$$
$$\mathrm{C(s)} + \mathrm{O} \rightarrow \mathrm{CO}, \tag{S2}$$
$$\mathrm{C(s)} + \mathrm{O} + \mathrm{O} \rightarrow \mathrm{C(s)} + \mathrm{O_2}, \tag{S3}$$
$$\mathrm{C(s)} + \mathrm{N} \rightarrow \mathrm{CN}, \tag{S4}$$
$$\mathrm{N} + \mathrm{N(s)} \rightarrow \mathrm{N_2}, \tag{S5}$$
$$\mathrm{C(s)} \rightarrow \mathrm{C}, \tag{S6}$$
$$2\mathrm{C(s)} \rightarrow \mathrm{C_2}, \tag{S7}$$
$$3\mathrm{C(s)} \rightarrow \mathrm{C_3}. \tag{S8}$$

Surface reactions (S1) and (S2) model finite-rate oxidation of the solid graphite, while reaction (S3) represents atomic oxygen surface recombination. Surface reactions (S4) and (S5) correspondingly model nitridation and atomic nitrogen surface recombination, respectively. Surface reactions (S6)-(S8) model sublimation of the solid graphite substrate. Reaction rates and parameterizations of κ_γ for each of the surface processes are evaluated, consistent with the formulations of Park (1976) for oxidation and O_2 recombination and Driver & MacLean (2011) for nitridation and N_2 recombination. A Knudsen–Langmuir formulation is used to evaluate the sublimation rates, consistent with Palmer & Shelef (1968), Baker (1976), and Keenan & Candler (1994).

Summation of the surface chemical production rates over all species α provides the following relation for the wall-normal velocity at the ablative surface,

$$\boldsymbol{u} \cdot \widehat{\boldsymbol{n}} = \frac{1}{\rho} \sum_{\alpha=1}^{N_s} \dot{\Omega}_\alpha, \tag{2.5}$$

which, upon substitution into Eq. (2.3), provides a closed-form surface continuity condition for each species, evaluated solely in terms of the partial densities, diffusion velocity, and surface production rates as

$$\frac{\rho_\alpha}{\rho} \sum_{\beta=1}^{N_s} \dot{\Omega}_\beta + \rho_\alpha \left(\boldsymbol{V}_{\boldsymbol{\alpha}} \cdot \widehat{\boldsymbol{n}} \right) = \dot{\Omega}_\alpha, \tag{2.6}$$

thereby providing an implicit boundary condition for the chemical concentration at the ablative wall. In particular, to infer the surface chemical concentrations at the ablative surface for the multicomponent Navier–Stokes solver, an N_s-dimensional Newton–Raphson method is employed at each point on the wall at each time step to satisfy Eq. (2.6) for the first $N_s - 1$ species, with the last residual associated with inviscid conservation of wall-normal momentum per Thompson & Gnoffo (2008). Convergence of the iterative method provides the partial density of each species at the wall, which can then be used in conjunction with Eq. (2.5) to set Dirichlet boundary conditions for the mole fractions and wall-normal velocity at the surface.

The overall physical configuration for the present DNS, represented schematically in Figure 1, comprises a noncatalytic hypersonic wedge with a semiangle of 16° and subsequent development of a turbulent boundary layer over a noncatalytic wall, followed by the ablative graphite surface considered herein. As such, the incoming turbulent boundary layer for the present DNS is specified at each time step by temporally interpolating a primitive database at the spanwise plane of $\hat{x} = 916$ from the noncatalytic boundary layer simulation of Williams *et al.* (2025). Spatial interpolation is not performed because

the spanwise and wall-normal extent, as well as spacing, of this study's computational grid is precisely that of the noncatalytic boundary layer. That is, the simulation domain for the present DNS extends $70\delta_0^*, 14\pi\delta_0^*$, and $40\delta_0^*$ in the streamwise, spanwise, and wall-normal directions, respectively, where δ_0^* is the displacement thickness of the upstream laminar boundary layer defined by Williams *et al.* (2023). Discretization of this domain is performed with 992, 1184, and 464 points in the streamwise, spanwise, and wall-normal directions, respectively. The inflow to the primary computational domain for this investigation, which substitutes the underlying noncatalytic surface with ablative graphite, provides a turbulent boundary layer with friction Reynolds and Mach numbers of $Re_\tau \simeq 1200$ and $Ma_\tau \simeq 0.2$. Owing to the elevated temperatures present in the aerodynamic heating layer, significant dissociation of O_2 gives rise to a near-wall molar fraction of atomic oxygen reaching 0.27 in the mean. In the noncatalytic boundary layer, turbulent mixing of this atomic oxygen produced a significant turbulence–chemistry interaction with the Zel'dovich exchange processes (Williams *et al.* 2024), and as shown in the next subsection, turbulent gas–surface interaction between the O radicals and the ablative graphite surface strongly modifies both gas-phase processes as well as producing strongly nonuniform surface ablation rates. Owing to the significant separation of timescales associated with the recession of the surface and of eddy turnover in the boundary layer, as reflected in Figure 2(d), this study does not consider solid deformation of the ablative wall. Therefore, long-duration, two-way coupling of the turbulent reacting hydrodynamics with the corresponding solid response is deferred to future work.

3. Results

Interaction between turbulent fluctuations and surface chemical processes in the Mach 7 hypersonic boundary layer gives rise to strongly nonuniform chemical composition and wall-normal mass flux, as reflected in Figure 2. In particular, mixing of atomic radicals with the graphite surface by turbulent structures gives rise to significant variation in the effective surface recession rate, with local rates of ablation varying by more than an order of magnitude along the wall. In the mean, the gas–surface interaction produces significant densities of carbon monoxide in the near-wall region via oxidation reactions, affecting both the mean near-wall temperature and the overall fluid density, as shown in Figures 3 and 4. In particular, in comparison to the counterpart boundary layer flow over a noncatalytic surface, the ablative turbulent boundary layer exhibits relatively higher Favre-averaged temperatures and densities. As the ablative configuration retains the same isothermal wall temperature as the noncatalytic case, this variation in the near-wall temperature arises not from the exchange of sensible and chemical energy via surface chemistry as in a surface energy-balance but instead from a combination of Eckert-number effects and gas-phase processes; the higher density for $y/\delta < 10^{-1}$ can be attributed to the additional mass in the flow produced primarily via oxidation of the graphite surface, where δ is the local displacement thickness of the turbulent boundary layer.

In addition to the effects imparted to the mass density and temperature fields, the compositional structure of the boundary likewise proves to be strongly affected by the turbulent gas–surface interaction, as shown in Figures 4 and 5. With the near-wall concentrations of atomic oxygen radicals strongly depleted by surface chemical processes relative to the noncatalytic boundary layer as a result of surface oxidation and recombination reactions, the molar fraction of carbon monoxide at the surface ultimately exceeds

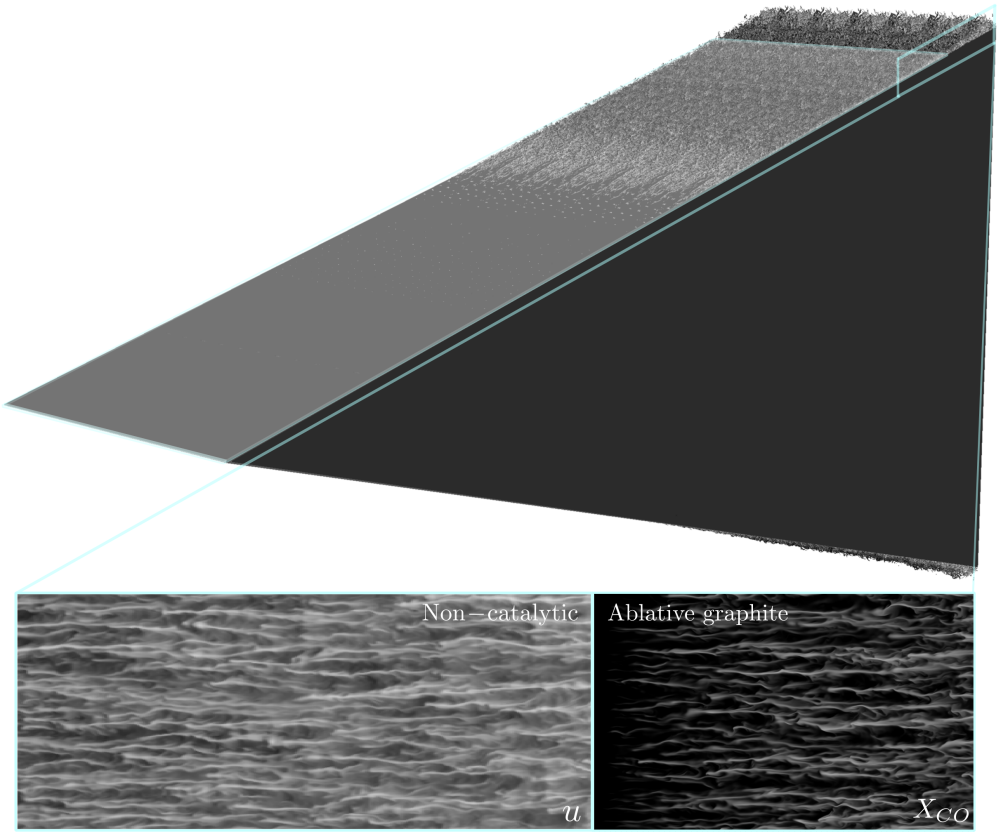

FIGURE 1. Composite schematic of the overall numerical experiment, composed of a noncatalytic hypersonic wedge (semiangle of 16°) and the turbulent boundary layer from Williams *et al.* (2025), together with the embedded ablative graphite substrate. The insets depict the instantaneous streamwise velocity and carbon monoxide contours on either side of the exchange location between the noncatalytic and ablative computations.

0.20. For the near-wall thermodynamic conditions in the hypersonic boundary layer, the production of other carbonaceous species ($\mathrm{C}, \mathrm{C_2}, \mathrm{C_3}, \mathrm{CN}$, and $\mathrm{CO_2}$) proves limited, with the Favre-averaged molar fraction of each species remaining below 10^{-3}. In addition to the direct production of carbon-containing species at the graphite surface, the gas–surface interaction indirectly modifies the densities of diatomic species by eliminating gas-phase radicals that enter into the Zel'dovich reactions. Consequently, the ablative boundary layer exhibits higher near-wall concentrations of both molecular oxygen and nitric oxide relative to its noncatalytic counterpart.

With respect to the variance of molar fraction fluctuations, turbulent mixing of ablation products away from the graphite surface gives rise to a peak in CO_x molar fraction variance that progresses outward, reaching $y/\delta \simeq 6 \times 10^{-2}$ by $\hat{x} = 985$. In contrast, the peaks in variance for the air–species molar fractions approximately retain their same off-wall locations as in the noncatalytic boundary layer of $y/\delta \simeq 10^0$ for $\mathrm{O_2}$, NO, and O and $y/\delta \simeq 10^{-1}$ for N. Owing to mean depletion of near-wall atomic oxygen by surface

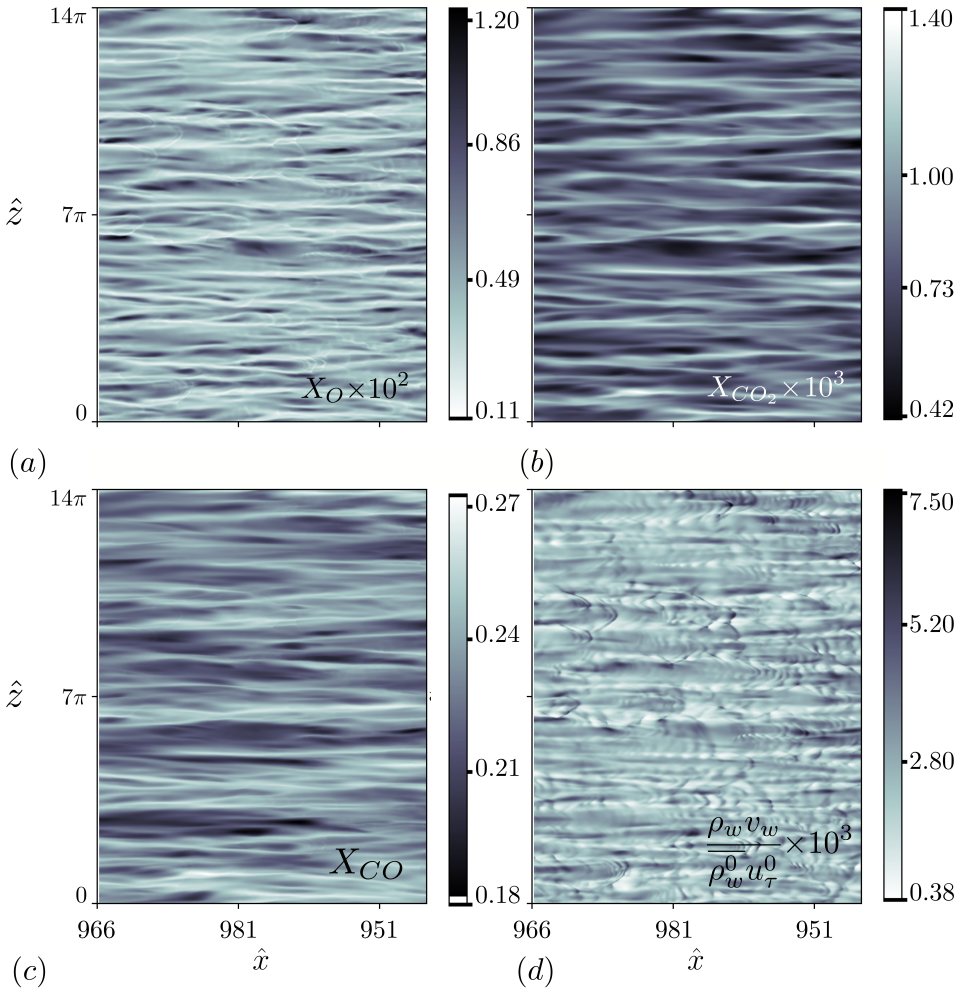

FIGURE 2. Molar fraction contours along the ablative graphite surface, where $\hat{(\cdot)}$ denotes normalization by the displacement thickness of the upstream laminar boundary layer. Molar fractions of (a) O, (b) CO, and (c) CO_2. (d) Net normalized ablative mass flux due to oxidation, nitridation, and sublimation processes, where $\overline{\rho_w^0}$ and u_τ^0 denote the mean density at the wall and the friction velocity of the incoming turbulent boundary layer as developed over the noncatalytic surface.

chemistry, however, a second inner peak in the O molar fraction variance is produced by the gas–surface interaction. This behavior in the O compositional variance resembles the spatial variation of temperature and atomic nitrogen variance in the near-wall region, consistent with turbulent mixing across a nonmonotonic mean flow.

The depletion of radical species by surface processes, particularly atomic oxygen, in the inner part of the boundary layer ultimately modifies the gas-phase chemical activity for all major air species to a significant degree, as shown in Figure 6. In particular, without the elevated concentrations of atomic oxygen required in the forward and backward directions of the first and second Zel'dovich exchange reactions, respectively, the near-wall

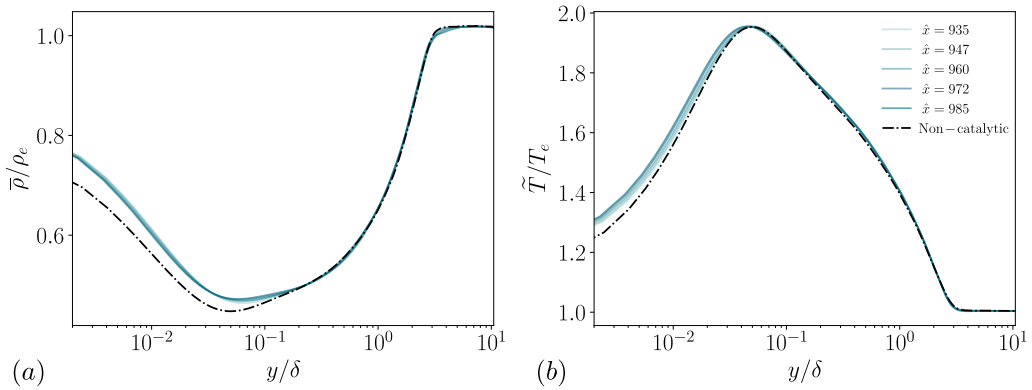

FIGURE 3. Wall-normal profiles of (a) Reynolds-averaged density and (b) Favre-averaged temperature.

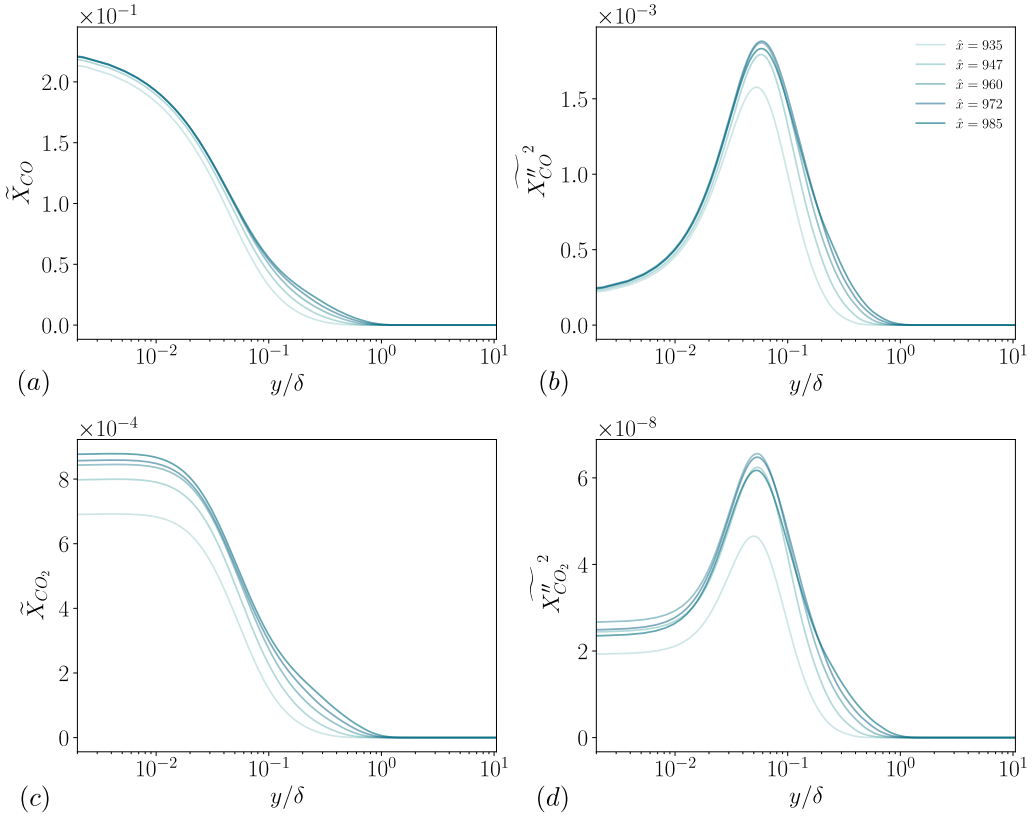

FIGURE 4. Favre average and root mean square of density-weighted fluctuations for the molar fractions of (a, b) carbon monoxide and (c, d) carbon dioxide.

production of molecular nitrogen is appreciably diminished relative to the noncatalytic boundary layer. Correspondingly, the near-wall production rates of both nitric oxide and atomic nitrogen are reduced substantially as well. The modulation of the near-wall thermodynamic states by gas–surface interaction likewise affects the production of atomic and molecular oxygen as mediated by both dissociation/recombination phenomena and

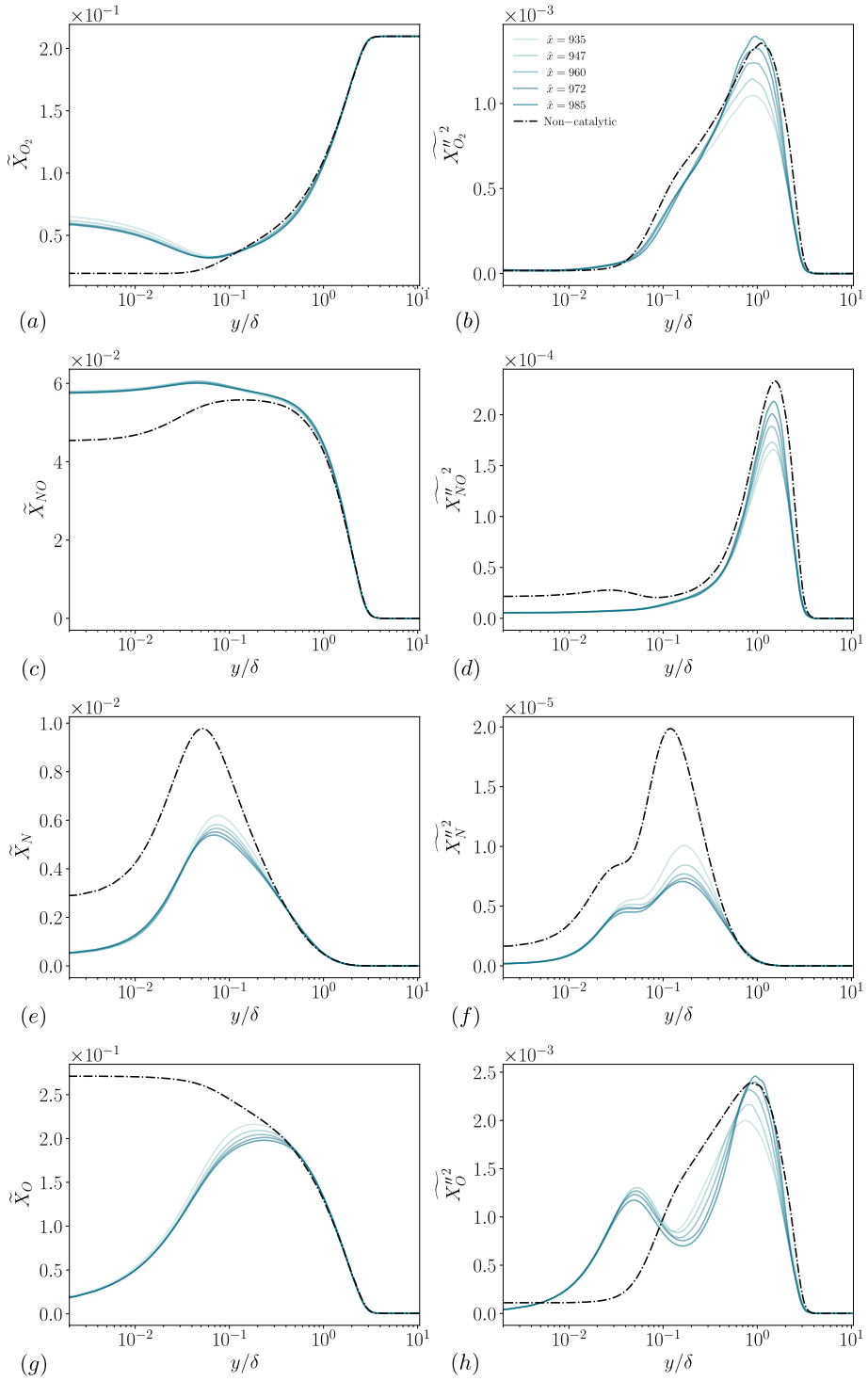

FIGURE 5. Favre average and root mean square of density-weighted fluctuations for the molar fractions of (a, b) molecular oxygen, (c, d) nitric oxide, (e, f) atomic nitrogen, and (g, h) atomic oxygen.

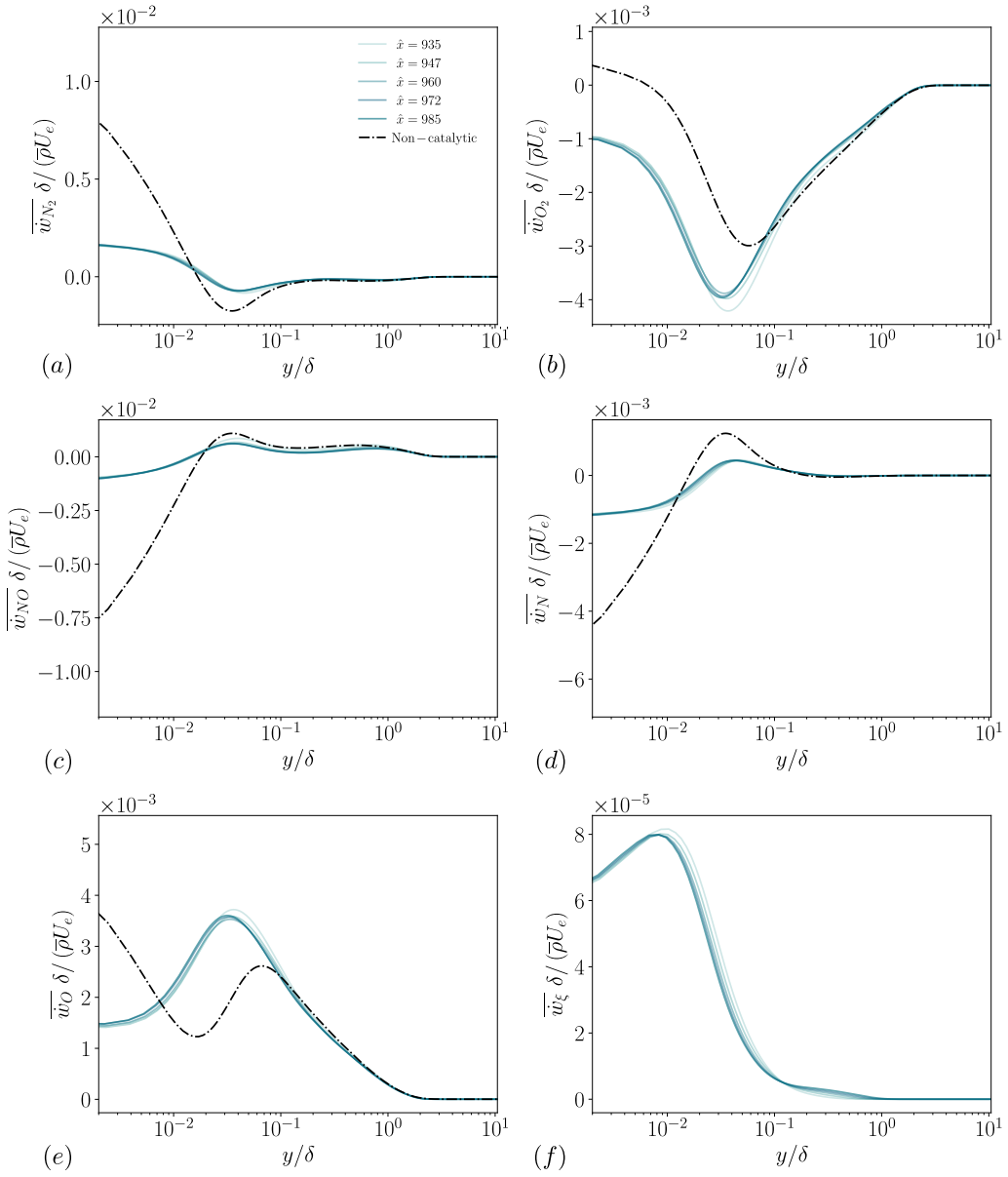

FIGURE 6. Reynolds-averaged net chemical production rate for (a) molecular nitrogen, (b) molecular oxygen, (c) nitric oxide, (d) atomic nitrogen, and (e) atomic oxygen, together with the averaged net gas-phase production rate of carbonaceous chemical species, $\dot{w}_\xi = \sum_\beta \dot{w}_\beta, \beta \in \{\mathrm{C}, \mathrm{C_2}, \mathrm{C_3}, \mathrm{CN}, \mathrm{CO}, \mathrm{CO_2}\}$.

the Zel'dovich mechanism. In particular, the peak in atomic oxygen production ultimately shifts outward in the boundary layer owing to gas–surface interaction, whereas the net depletion of molecular oxygen is augmented substantially for $y/\delta \lesssim 10^{-1}$. While the gas-phase chemical activity of the oxygenic species is ultimately heightened by ablation in the turbulent boundary layer, particularly for $10^{-2} \lesssim y/\delta \lesssim 10^{-1}$, the ablation products themselves largely prove chemically frozen. The net gas-phase chemical production rate

of carbonaceous species, depicted in Figure 6(f), remains approximately 50 times lower than that of oxygenic air species. As such, treatment of the gas-phase ablation products as inert at these thermodynamic conditions may be warranted.

4. Conclusions

In order to characterize the mutual interactions between compressible turbulence, gas-phase aerothermochemistry, and gas–surface processes in high-Mach-number, high-enthalpy flows, we have presented preliminary DNS results for a turbulent hypersonic boundary layer overriding an ablative graphite surface. To capture departures from chemical equilibrium, the numerical solution of species-continuity equations provides finite-rate evolution of not only the air species N_2, O_2, NO, N, and O but also the ablation products C, C_2, C_3, CN, CO, and CO_2. The surface chemical mechanism for graphite ablation comprises oxidation, nitridation, recombination, and sublimation processes, while the gas-phase processes considered include both dissociation/recombination phenomena and exchange reactions between the air and carbon-containing species. Due to a combination of turbulence-induced compositional and pressure fluctuations on the wall, the implied surface recession rate varies instantaneously by more than an order of magnitude. With respect to the mean flow, almost all atomic radical species in the near-wall region are ultimately depleted via surface chemical reactions, giving rise to a near-wall carbon monoxide layer that diffuses outward via molecular and ultimately turbulent mixing. Owing to these significant compositional variations imparted by the turbulent gas–surface interactions, the gas-phase chemical reaction rates are distorted relative to those in the noncatalytic boundary layer, strongly modulating the net gas-phase chemical production of all air species.

Acknowledgments

C.T.W. acknowledges support from the National Science Foundation Graduate Research Fellowship Program under grant DGE-2146755. This investigation was funded by the Advanced Simulation and Computing program of the US Department of Energy's National Nuclear Security Administration via the PSAAP-III Center at Stanford under grant DE-NA0003968. The authors thank Dr. Salvador Gomez for his thorough review of this brief.

REFERENCES

Baker, R. 1976 Graphite ablation chemistry nonequilibrium effects. *AIAA Paper 1975-735* .

Bertin, J. J. & Cummings, R. M. 2006 Critical hypersonic aerothermodynamic phenomena. *Annu. Rev. Fluid Mech.* **38**, 129–157.

Bianchi, D., Nasuti, F. & Martelli, E. 2010 Navier–Stokes simulations of hypersonic flows with coupled graphite ablation. *J. Spacecr. Rockets* **47**, 554–562.

Candler, G. V. 2019 Rate effects in hypersonic flows. *Annu. Rev. Fluid Mech.* **51**, 379–402.

Canning, T. N., Chapman, G., Tauber, M. & Wilkins, M. 1968*a* Orderly three-dimensional processes in turbulent boundary layers on ablating bodies. Tech. Memo. 19680024963, NASA Ames Research Center .

Canning, T. N., Tauber, M. E. & Wilkins, M. E. 1968*b* Ablation patterns on cones having laminar and turbulent flows. *AIAA J.* **6**, 174–175.

Di Renzo, M., Fu, L. & Urzay, J. 2020 HTR solver: an open-source exascale-oriented task-based multi-GPU high-order code for hypersonic aerothermodynamics. *Comput. Phys. Commun.* **255**, 107262.

Driver, D. & MacLean, M. 2011 Improved predictions of PICA recession in arc jet shear tests. *AIAA Paper 2011-141* .

Engel, C. D., Farmer, R. C. & Pike, R. W. 1973 Ablation and radiation coupled viscous hypersonic shock layers. *AIAA J.* **11**, 1174–1181.

Gnoffo, P. A., Johnston, C. O. & Thompson, R. A. 2010 Implementation of radiation, ablation, and free energy minimization in hypersonic simulations. *J. Spacecr. Rockets* **47**, 251–257.

Gottlieb, S., Shu, C.-W. & Tadmor, E. 2001 Strong stability-preserving high-order time discretization methods. *SIAM Rev.* **43**, 89–112.

Keenan, J. & Candler, G. 1994 Simulation of graphite sublimation and oxidation under re-entry conditions. *AIAA Paper 1994-2083* .

Komurasaki, K. & Candler, G. V. 2000 Laminar-to-turbulent transitions over an ablating reentry capsule. *Acta Astronaut.* **47**, 745–751.

Laganelli, A. & Nestler, D. 1969 Surface ablation patterns—a phenomenology study. *AIAA J.* **7**, 1319–1325.

Lin, T., Sproul, L., Kim, M., Olmos, M. & Feiz, H. 2006 Hypersonic reentry vehicle wake flow fields at angle of attack. *AIAA Paper 2006-582* .

Martin, A. & Boyd, I. D. 2015 Strongly coupled computation of material response and nonequilibrium flow for hypersonic ablation. *J. Spacecr. Rockets* **52**, 89–104.

McQuaid, J. A., Brehm, C., Zibitsker, A. L. & Martin, A. 2025 Development of an overset near-body Cartesian solver for graphite ablation simulations. *AIAA J.* **63**, 1–23.

Miró, F. M. & Pinna, F. 2020 Injection-gas-composition effects on hypersonic boundary-layer transition. *J. Fluid Mech.* **890**, R4.

Miró, F. M. & Pinna, F. 2021 Decoupling ablation effects on boundary-layer stability and transition. *J. Fluid Mech.* **907**, A14.

Morkovin, M. V. 1969 Critical evaluation of transition from laminar to turbulent shear layers with emphasis on hypersonically traveling bodies. Tech. Rep., Air Force Flight Dynamics Laboratory .

Mortensen, C. H. & Zhong, X. 2014 Simulation of second-mode instability in a real-gas hypersonic flow with graphite ablation. *AIAA J.* **52**, 1632–1652.

Mortensen, C. H. & Zhong, X. 2016 Real-gas and surface-ablation effects on hypersonic boundary-layer instability over a blunt cone. *AIAA J.* **54**, 980–998.

Olynick, D., Chen, Y.-K., Tauber, M., Olynick, D., Chen, Y.-K. & Tauber, M. 1997 Forebody TPS sizing with radiation and ablation for the Stardust sample return capsule. *AIAA Paper 1997-2474* .

Palmer, H. B. & Shelef, M. 1968 Vaporization of carbon. *Chem. Phys. Carbon* **4**, 85–135.

Park, C. 1976 Effects of atomic oxygen on graphite ablation. *AIAA J.* **14**, 1640–1642.

Park, C. 1990 *Nonequilibrium Hypersonic Aerothermodynamics*. Wiley.

Park, C., Howe, J. T., Jaffe, R. L. & Candler, G. V. 1994 Review of chemical-

kinetic problems of future NASA missions. II. Mars entries. *J. Thermophys. Heat Transf.* **8**, 9–23.

Schneider, S. P. 2008 Effects of roughness on hypersonic boundary-layer transition. *J. Spacecr. Rockets* **45**, 193–209.

Schneider, S. P. 2010 Hypersonic boundary-layer transition with ablation and blowing. *J. Spacecr. Rockets* **47**, 225–237.

Stock, H. W. 1973 Cross-hatching: a comparison between the behaviour of liquefying and subliming ablation materials. Tech. Rep., von Karman Institute for Fluid Dynamics .

Thomas, P. & Neier, K. 1990 Navier–Stokes simulation of three-dimensional hypersonic equilibrium flows with ablation. *J. Spacecr. Rockets* **27**, 143–149.

Thompson, R. & Gnoffo, P. 2008 Implementation of a blowing boundary condition in the LAURA code. *AIAA Paper 2008-1243* .

Urzay, J. 2018 Supersonic combustion in air-breathing propulsion systems for hypersonic flight. *Annu. Rev. Fluid Mech.* **50**, 593–627.

Urzay, J. & Di Renzo, M. 2021 Engineering aspects of hypersonic turbulent flows at suborbital enthalpies. *Annual Research Briefs*, Center for Turbulence Research, Stanford University, pp. 7–32.

Vincenti, W. G. & Krüger, C. H. 1965 *Introduction to Physical Gas Dynamics*. Wiley.

Williams, C. T., Di Renzo, M. & Moin, P. 2022 Computational framework for direct numerical simulation of shock–turbulence interaction in thermochemical nonequilibrium. *Annual Research Briefs*, Center for Turbulence Research, Stanford University, pp. 203–216.

Williams, C. T., Di Renzo, M. & Moin, P. 2023 Direct simulation of turbulence–chemistry interaction in a strongly reacting turbulent hypersonic boundary layer. *Annual Research Briefs*, Center for Turbulence Research, Stanford University, pp. 173–184.

Williams, C. T., Di Renzo, M. & Moin, P. 2024 Statistical decomposition of turbulence–chemistry interactions in a hypersonic boundary layer. *Annual Research Briefs*, Center for Turbulence Research, Stanford University, pp. 79–92.

Williams, C. T., Di Renzo, M. & Moin, P. 2025 Turbulence–chemistry interaction in a non-equilibrium hypersonic boundary layer. *J. Fluid Mech.* **1017**, A30.

Zel'dovich, Y. B. & Raizer, Y. P. 2002 *Physics of Shock Waves and High-Temperature Hydrodynamic Phenomena*. Dover.